Green synthesis of Layered Double Hydroxides (LDH) for the remediation of As and Cd in water and soil

Xuanru Li[a], Liuwei Wang[a], Bei Chen[b], Yuanyuan Xu[b], Huixia Wang[a], Fei Jin[c], Zhengtao Shen[d], Deyi Hou[a,*]

[a] School of Environment, Tsinghua University, Beijing 100084, China

[b] Guangxi Zhuang Autonomous Region Ecological and Environmental Monitoring Centre, Nanning 530028, China

[c] School of Engineering, Cardiff University, CF24 3AA, UK

[d] School of Earth and Engineering Sciences, Nanjing University, Nanjing 210023, China

*corresponding author (houdeyi@tsinghua.edu.cn)

Phone: +86-010-62781159

Abstract

Layered double hydroxides (LDH) show great promise for the remediation of heavy metals and metalloids in aqueous media and soils. In this study, we propose a green synthesis approach for LDH utilizing industrial waste granulated ground blast furnace slag (GGBS) and readily available magnesium oxide (MgO), and applied these green synthesized LDH for As and Cd remediation in both water and soil. The synthesized LDH were characterized via multiple approaches including SEM, HRTEM-EDS, TGA, XRD, and FTIR, demonstrating that the addition of 20% MgO in the raw materials (LDH_b) substantially improved the stability of LDH compared to LDH synthesized solely from pure GGBS (LDH_a). Batch adsorption experiments were conducted to evaluate the adsorption efficiency of LDH_a and LDH_b for Cd(II) and As(V) under varying initial solution pH conditions. Results showed that as the pH increased, calcium leaching remained high while aluminum leaching gradually increased. The adsorption isotherms and kinetic studies further revealed that LDH_b displayed better adsorption performance for As(V) across different pH conditions, while both LDH showed a 100% removal rate of Cd(II) at pH ranging from 6 to 9. Both LDH_a and LDH_b exhibited promising immobilization effects on As and Cd in contaminated soils, with LDH_a showing superior stabilization performance toward As, immobilizing 83.8% of bioavailable As in the farmland soil and 78.7% in the industrial site soil, compared to LDH_b's 54.8% and 50.6%,

respectively. The findings of this study hold promise for the practical application of LDH as an efficient and environmentally friendly remediation material for contaminated water and soils containing toxic metal(loid)s.

Keywords: LDH, Green synthesis, GGBS, Adsorption, Soil remediation.

1 Introduction

Layered double hydroxides (LDH), also known as anionic clays, are a type of clay mineral widely present in nature but can also be synthetically prepared (Guan et al., 2022). They possess a general formula of $[M^{2+}_{1-x} M^{3+}_{x} (OH)_2]^{x+} A^{n-}_{x/n} \cdot mH_2O$. LDH consist of stacked layers resembling brucite $M^{2+}(OH)_2$, wherein a portion of M^{2+} ions are replaced by M^{3+} ions, resulting in a positively charged interlayer (Ye et al., 2022). To maintain charge balance, charge-compensating anions (A^{n-}) are incorporated into the interlayer (Newman et al., 2002; Shen et al., 2020). Due to their alkaline nature and positively charged layered structure, LDH have the ability to exchange hazardous anions (Peligro et al., 2016) and act as acid buffers to precipitate heavy metal cations in aqueous solutions (Liang et al., 2013; Rojas, 2014). LDH are classified into various categories, such as Mg/Al-LDH, Ca/Al-LDH, Mg/Fe-LDH, Cu/Al-LDH, among others, with Mg/Al and Ca/Al LDH being the most common (Tran et al., 2018; Hudcova et al., 2019; Missau et al., 2021; Yuan et al., 2021).

Despite LDH demonstrating outstanding potential for remediating contaminated water and soil, the utilization of chemical reagents during the synthesis process has led to intensive energy consumption and depletion of natural resources (Wang et al., 2019; Hou et al., 2023). This critical issue has hindered its large-scale practical application in environmental remediation. Therefore, synthesizing LDH materials through a green and sustainable approach has

become imperative (Wang et al., 2022b; Jaworski et al., 2023). In recent years, with the rise of green and sustainable remediation (GSR), developing new materials based on industrial solid waste for soil and water remediation has emerged as a new trend (Wang et al., 2021; Hou, 2022; Wang et al., 2023a). GSR aims to conserve energy and resources while maximizing both economic and environmental benefits in material manufacturing and application (Hou, 2021; Jin et al., 2021; Hou, 2023).

Industrial wastes show much promise for the green synthesis of engineered materials like LDH. Granulated ground blast furnace slag (GGBS), an abundant byproduct from the ironmaking industry with annual production of several hundred million tons worldwide, has been widely used as a source of metal oxides for material production (Siddique and Iqbal Khan, 2011; Guo et al., 2019). GGBS mainly contains alkali earth metals (i.e., calcium and magnesium), aluminum, and silicon, making it a potential raw material for adsorbents like porous silica, zeolites, and LDH (Yi et al., 2016; Vollpracht et al., 2018). In this study, we develop a green synthesis method that converts GGBS into LDH. To enhance stability and applicability in contaminated water and soil remediation, we also introduce magnesium oxide (MgO), derived from low-temperature calcination of magnesite, as a raw material with GGBS to synthesize CaMg/Al-LDH. We then investigate the removal efficiency of cadmium (Cd) and arsenic (As) from aqueous solutions using LDH synthesized under different raw material compositions. Finally, we explore the stabilization performances of

LDH for Cd and As in contaminated soils collected from an agricultural field and an industrial site, respectively.

2 Materials and methods

2.1 Green synthesis of LDH

GGBS and MgO were obtained from WuGang and Wuhan Sanyuan Companies, China, respectively. The raw materials were ground and sieved with 200 mesh prior to use. The chemical compositions of GGBS and MgO determined by X-ray fluorescence (XRF, ARL PERFORM X, Thermo Fisher, USA) were listed in Table S1. GGBS mainly consists of 49.03 wt% CaO, 26.90 wt% SiO_2, 6.51 wt% MgO, and 13.17 wt% Al_2O_3, with the molar ratios of Ca/Al and Mg/Al of 3.39 and 0.63, respectively. Cadmium nitrate ($Cd(NO_3)_2$) from Aladdin Industrial Corporation is of analytical-grade and sodium arsenate heptahydrate ($Na_2HAsO_4 \cdot 7H_2O$) with purity of >98% was purchased from Sigma-Aldrich.

The LDH were synthesized through the acid-leaching and co-precipitation method (Fig. 1). (For simplicity, LDH is used to represent the adsorbent as it is the primary phase, although various impurities may be present). To effectively extract Ca, Mg, and Al ions from GGBS and MgO while minimizing the presence of Si, preliminary experiments were conducted to determine the optimal experimental parameters, such as the concentration of hydrochloric acid in the

leaching solution, solid-liquid ratio, and leaching temperature. The specific synthesis steps were as follows: 10 grams of the raw solid materials with varying mass proportions (refer to Table S2) were dissolved in 200 mL of a 3 M HCl aqueous solution. The dispersion was mixed using a magnetic hotplate (HJ-4A, Kexi Instrument Co. Ltd., Changzhou, China) at 600 rpm and 80°C for 4 hours. Subsequently, the mixture underwent vacuum filtration (SHZ-D-III, Lingke industrial development Co. Ltd., Shanghai, China). Dropwise addition of a 4 M NaOH solution to the collected filtrate with vigorous stirring was carried out until the pH of the dispersion stabilized at approximately 11.5. The resulting slurry was covered and aged at 80°C for 24 hours to facilitate crystallization. Afterward, the slurry was collected, washed with deionized water, and dried overnight at approximately 100°C to obtain the primary LDH. Finally, all samples were sealed in centrifuge tubes and stored in a desiccator.

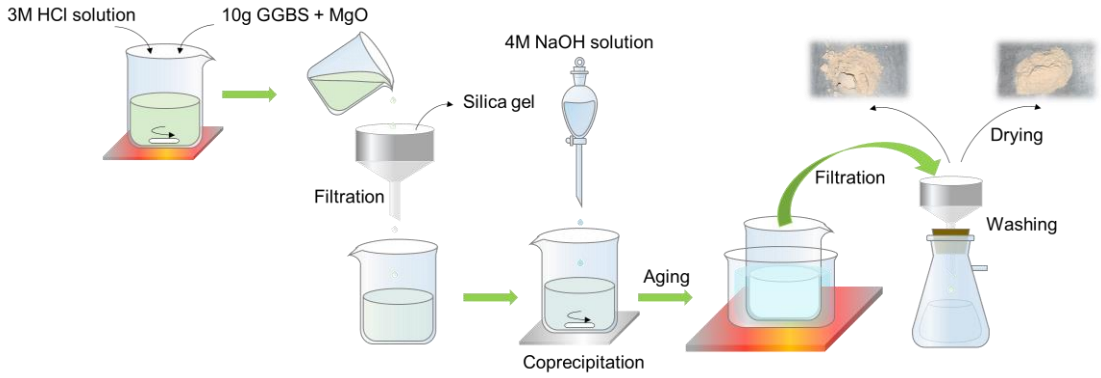

Fig. 1. Schematic diagram of the green synthesis procedure of LDH from GGBS and MgO.

2.2 Characterization of LDH

To investigate the crystal structure of the samples, X-ray diffraction (XRD) patterns were obtained using a Rigaku D/max-2500 diffractometer equipped with Cu Kα radiation (λ = 0.15406 nm). The scanning rate was set at 5 °/min, with a step size of 0.02 ° over the 2θ range from 3 ° to 80 °. The morphology and surface elemental composition of the synthesized materials were examined using field emission scanning electron microscopy (FE-SEM, SU8010, Hitachi, Japan) and high resolution transmission electron microscopy (HRTEM, JEM-2010, JEOL, Japan). The N_2 adsorption-desorption isotherms at 77 K were determined using a Quadasorb SI-MP instrument (USA). Subsequent to degassing the LDH samples under heating conditions at 373 K for a duration of 11 hours, the specific surface area was computed through the MultiPoint Brunauer-Emmett-Teller (BET) method within the relative pressure range of 0.10–0.30 on the adsorption-desorption branch. The assessment of pore size distribution was conducted utilizing the Barrett-Joyner-Halenda (BJH) method based on the N_2 adsorption isotherm. The total pore volume was calculated for pores with diameters less than a specified value of P/P_0, approximately 0.9935. Thermogravimetric analysis (TGA, Q5000 IR, TA Instruments, USA) was performed in air, with a heating rate of 10°C/min, over a temperature range of 50°C to 950°C. Fourier transform infrared spectra (FTIR, VERTEX 70, Bruker, Germany) were obtained using the KBr pellet method to characterize the functional groups, covering a wavenumber range of 400–4000 cm^{-1}. XPS

147 spectra of the LDH were performed by an X-ray photoelectron spectroscopy
148 (250 Xi, Thermofisher, USA) with the monochromatic Al Kα Xray radiation. The
149 chemical compositions of the synthesized LDH were determined using X-ray
150 fluorescence (XRF) analysis. Prior to characterization, all samples were dried
151 at 60°C for 24 hours.
152

153 ## 2.3 Adsorption of Cd and As from water

154 Batch adsorption experiments were conducted at room temperature to
155 investigate the removal performance of as-synthesized LDH for Cd and As. The
156 stock solutions of various Cd or As concentrations were prepared by dissolving
157 predetermined amounts of $Cd(NO_3)_2$ and $Na_2HAsO_4 \cdot 7H_2O$ in deionized water
158 followed by dilution in measuring flasks, respectively. The batch adsorption
159 studies were conducted in 50 mL plastic centrifuge tubes. For the Cd(II) solution,
160 0.01 g of LDH was added to a 40 mL volume, while for the As(V) solution, 0.033
161 g of LDH was added to a 20 mL volume. This resulted in a solid-liquid ratio of
162 1:4000 for Cd(II) and 1:600 for As(V). The adsorption performance of LDH_a and
163 LDH_b was examined at varying initial pH levels (Cd: 2-9; As: 2-12). Adsorption
164 kinetics experiments were conducted for both materials on Cd and As under
165 specific conditions. The initial pH of the Cd solution was set at 5.3, while the
166 initial pH of the As solution was set at 8. The initial concentrations of Cd and As
167 were both maintained at 100 ppm. Samples were collected at regular intervals

of 10 min, 30 min, 45 min, 1 h, 3 h, 6 h, 24 h, 48 h, and 72 h. In the adsorption isotherm experiments, the initial pH of the Cd solution was adjusted to 5, and the initial pH of the As solution was adjusted to 7. The initial concentrations of Cd and As were varied within the range of 25 ppm, 50 ppm, 100 ppm, 200 ppm, and 300 ppm. Samples were collected once the adsorption reached equilibrium for each concentration. After adding the solid material to the aqueous solution, the centrifuge tube was tightly sealed and placed in a water bath isothermal shaker, where it was shaken at 200 rpm and maintained at a temperature of 25 °C. Following the oscillation, the slurry was filtered using a 0.22 μm syringe filter to determine the concentration of Cd and As in the supernatant. This analysis was performed using an inductively coupled plasma optical emission spectrometer (ICP-OES, Optima 8000, PerkinElmer, USA). If required, dilution of the supernatant was carried out using 1% HNO_3.

The adsorption capacities of the LDH for Cd(II) and As(V) were calculated by the following equation (Eq. (1)):

$$q_e = (C_0 - C_e)\frac{V}{m} \quad (1)$$

where q_e is solid-phase metal ion concentration at equilibrium (mg g^{-1}), C_0 and C_e represent the initial and equilibrium liquid-phase metal ion concentrations (mg L^{-1}), respectively. V refers to the solution volume (L), and m the mass of the solid (g). Details regarding adsorption isotherm and kinetics modeling can be found in Text S1 of the supplementary information.

2.4 Immobilization of Cd and As in soil

In this study, we conducted an experiment to immobilize Cd and As in soil collected from farmland in Southwest China, and soil from an ore processing site in Southwest China. The soil samples underwent initial drying and sieving to achieve a particle size smaller than 2 mm. The soils were found to be enriched with Cd and As (Table 1). The soil pH values were determined following the procedures outlined in MEE (2018), employing a solid-to-liquid ratio of 1:2.5. Measurement of soil electrical conductivity (EC) values adhered to the guidelines of MEE (2016a), utilizing a solid-to-liquid ratio of 1:5. For the analysis of total concentrations of Cd and As we utilized ICP-MS after microwave digestion, in accordance with USEPA Method 3051A USEPA (2007). The total organic carbon content of the soils was measured using a TOC analyzer (multi N/C 3100, Analytik Jena GmbH, Germany). Furthermore, The particle size distribution of the soil was determined in the wet mode through a laser particle size analyzer (LS13320, Beckman Coulter Inc., US). The soil cation exchange capacity (CEC) was assessed using the hexaamminecobalt(III) chloride method, as per ISO (2018). The results of the tests are shown in Table 1.

Various dosages (1%, 3%, and 5%) of LDH were thoroughly mixed with 10 g of each soil sample in a dry state. Subsequently, water was added to achieve a

40% soil moisture content, and the soil samples were incubated in open containers. Additionally, a control group with 10 g of soil at 40% moisture content underwent incubation under identical conditions. After incubation periods of 3, 7, and 14 days, specific amounts of each soil sample were collected for subsequent analysis. The collected soil samples were then dried, ground to a size smaller than 0.15 mm, and subjected to soil pH testing (ST3100, Ohaus, USA). The mobility of Cd and As was assessed by conducting a water leaching test with a solid-to-liquid ratio of 1:10 (MEE, 2010) and a TCLP (Toxicity Characteristic Leaching Procedure) leaching test (US EPA, 1992). Additionally, the bioavailability of contaminants was determined through a DTPA (Diethylenetriaminepentaacetic Acid) extraction with a solid-to-liquid ratio of 1:2 (MEE, 2016b). Metal(loid) concentrations in the extractant were analyzed using ICP-MS (7800, Agilent, USA). The respective detection limits for Cd and As were 0.065 μg/L and 0.16 μg/L. The immobilization rate (IR) and the bioavailability decrease rate (BDR) were determined using the following equations (Eq. (2), (3)):

$$IR = \frac{c_{0,water/TCLP} - c_{i,water/TCLP}}{c_{0,water}} \times 100\% \quad (2)$$

$$BDR = \frac{c_{0,DTPA} - c_{i,DTPA}}{c_{0,DTPA}} \times 100\% \quad (3)$$

where $c_{0,water/TCLP}$ and $c_{0,DTPA}$ represent the concentrations of Cd and As in water/TCLP and DTPA leachates of the unamended soils; $c_{i,water/TCLP}$ and $c_{i,DTPA}$ represent the concentrations of Cd and As in water/TCLP and DTPA leachates of the amended soils.

230

231 **Table 1** Soil properties

Property	Value[a]	
	Agricultural soil	Industrial site soil
pH	7.73 ± 0.01	7.49 ± 0.01
TOC (g/kg)	24.99 ± 0.03	19.17 ± 0.03
CEC (cmol/kg)	18.55 ± 0.04	15.28 ± 0.02
Sand (%)	4.34 ± 0.71	17.75 ± 0.71
Silt (%)	72.80 ± 0.10	61.06 ± 0.47
Clay (%)	22.86 ± 0.63	21.18 ± 0.32
Texture	Silt loam	Silt loam
Total Cd (mg/kg)	13.28 ± 0.06	8.18 ± 0.34
Total As (mg/kg)	807.78 ± 5.85	1158.70 ± 9.51
Water extractable Cd (mg/kg)	0.033 ± 0.002	0.032 ± 0.002
Water extractable As (mg/kg)	4.84 ± 0.06	7.32 ± 0.10
DTPA extractable Cd (mg/kg)	4.51 ± 0.03	2.71 ± 0.03
DTPA extractable As (mg/kg)	1.92 ± 0.02	3.17 ± 0.03
TCLP extractable Cd (mg/kg)	4.66 ± 0.01	2.81 ± 0.04
TCLP extractable As (mg/kg)	14.04 ± 0.12	22.43 ± 0.33

232 [a] Mean ± standard deviation, n = 3.

233

2.5 Statistical analyses

The experiments were conducted in triplicates, and the standard errors were depicted as error bars in the figures. To test the differences among the groups, one-way analysis of variance (ANOVA) was employed, followed by the Fisher Least Significant Difference (LSD) test at a significance level of 0.05. Modeling and plotting were carried out using Origin 2023b software. X-ray diffraction (XRD) analysis was performed using X'Pert HighScore Plus 2.0. The analysis of the XPS test data results of the samples was conducted using CasaXPS 2.3.19PR1.0.

3 Results and discussion

3.1 Characteristics of green-synthesized LDH

Table S3 and S4 present the leaching quantities and leaching ratios of the primary elements (Ca, Mg, Al, Si) in the raw materials after acid leaching, along with the content and key molar ratios of the main elements in LDH. Upon comparing the molar ratios of M^{2+} and M^{3+} in the acid leaching solution with those observed in the synthesized LDH, a consistent trend emerges, indicating that the ratio in LDH consistently registers lower values than in the acid leaching solution. As an illustration, in the transition from the leaching solution of GGBS to LDH_a, the M^{2+} and M^{3+} molar ratio decreases from 3.39 to 2.65. Similarly, for LDH_b, it decreases from 4.82 to 3.57. It is widely acknowledged that a molar

ratio of M^{2+} and M^{3+} in LDH exceeding the range of 2 to 4 can lead to heightened structural instability (Cavani et al., 1991; Wang et al., 2009). This observation implies that, in the green synthesis route, the content of Al^{3+} in the raw materials is relatively scarce. The utilization efficiency of Al atoms throughout the entire synthesis process facilitates the calculation of LDH yield. Considering each batch of synthesis consumes 10 g of raw material and yields approximately 10 g of LDH, the calculated yield stands at approximately 90.9% for LDH_a and 91.3% for LDH_b. While the utilization efficiency of Al atoms in the synthesis processes of the two LDH is roughly comparable, an intriguing observation emerges: the Ca/Al ratio in LDH_b experiences a significant decrease, surpassing the reduction in Ca^{2+} acid leaching concentration as indicated in Table S3. This phenomenon can be attributed to the undersaturation of Al^{3+} in the green synthesis process outlined in this study for LDH, leading to a competitive interaction between Ca^{2+} and Mg^{2+} for Al^{3+}. Generally, during the co-precipitation synthesis of LDH, Ca/Al-LDH requires a higher pH of the reaction solution compared to Mg/Al-LDH (Sun et al., 2015; Gabriella Alexandre Borgesa et al., 2020; Xu et al., 2020; Zhang et al., 2022a). This can be explained by the greater solubility product constant of $Ca(OH)_2$ compared to $Mg(OH)_2$ ($K_{sp,Calcium\ hydroxide} = 5.02\times10^{-6} > K_{sp,Magnesium\ hydroxide} = 5.51\times10^{-12}$) (Lide, 2004). The gradual increase in pH during the co-precipitation step, coupled with the condition of Al^{3+} undersaturation in the reaction system, triggers a sequence where Mg^{2+} precipitates before Ca^{2+}. This sequence leads to a notable

276 decrease in the Ca/Al ratio in LDH_b compared to LDH_a.

277

278 The analysis of the N_2 adsorption-desorption isotherms reveals that LDH exhibit
279 a Type IV curve (Fig. S1), according to the IUPAC classification (IUPAC, 2015),
280 strongly indicating their mesoporous nature. The BJH pore size distribution,
281 calculated from the desorption data and shown in the inset graph of Fig. S1,
282 indicates average pore diameters of 1.94 nm for LDH_a and 2.20 nm for LDH_b,
283 primarily distributed within the mesoporous range of 1 to 20 nm. Notably, the
284 adsorption isotherms exhibit prominent hysteresis loops at relative pressures
285 (P/P_0) ranging from 0.4 to 1.0, suggesting the presence of numerous
286 mesopores formed by the accumulation of LDH nanosheets (Alothman, 2012;
287 He et al., 2015). Due to their porous structure, LDH_a and LDH_b demonstrate
288 substantial specific surface areas of 39.8 m^2/g and 32.5 m^2/g, respectively
289 (Table 2). This large specific surface area offers advantages in enhancing the
290 reactive area of LDH for heavy metal cations and anions, as well as providing
291 three-dimensional pathways for ion diffusion (Jing et al., 2018).

292 **Table 2** Porous structure of LDH.

Material	Specific surface area (m^2/g)	Total pore volume (cm^3/g)	Average pore diameter (nm)
LDH_a	39.8	0.250	1.94
LDH_b	32.5	0.116	2.20

293

Scanning Electron Microscope (SEM) and Transmission Electron Microscope (TEM) images were utilized to characterize the morphology and microstructure of both the raw material GGBS (Fig. S2) and the synthesized LDH. In Fig. 2(a, b), the SEM images reveal that despite varying synthesis conditions, the LDH exhibit individual crystal grains with obtuse boundaries, displaying a stacked plate-like structure at the micro scale. The lateral size of these plate-like structures ranges from several nanometers to tens of nanometers, and LDH_b's single-layered crystal appears thicker compared to LDH_a. In addition, High-resolution Transmission Electron Microscope (HRTEM) images (Fig. 2c, g) reveal that the synthesized LDH exhibit a morphology distinct from the raw material GGBS, with both LDH types displaying typical hexagonal and plate-like characteristics of LDH (Zhou et al., 2018). The crystal plate of LDH_b (approximately 500nm) is larger than that of LDH_a (approximately 300nm). This is consistent with LDH_a having a higher specific surface area (39.8 m^2/g) compared to LDH_b (32.5 m^2/g). Additionally, Energy-dispersive X-ray (EDX) spectroscopy elemental mapping shows a uniform distribution of Ca (Fig. 2d, h) and Al (Fig. 2f, j), while Mg is concentrated in specific regions (Fig. 2e, i), suggesting that Mg is less incorporated into the LDH structure compared to Ca. The concentrated regions may represent observed particles attached to the plate-like particles, likely impurities such as Portlandite, Periclase, etc., which generally have smaller particle sizes than hydrotalcite (Jiang et al., 2019; Zeng et al., 2022).

316

317 The X-ray diffraction (XRD) patterns of LDH reveal a distinct contrast to the
318 amorphous state of GGBS (Fig. S4), displaying a characteristic layered double
319 hydroxide structure (Fig. 2k). The patterns are characterized by sharp
320 reflections that correspond to the R3m rhombohedral symmetry (Bellotto et al.,
321 1996; Wang et al., 2009). Specifically, in LDH_a, the labeled basal planes (003),
322 (006), and (009), along with other peaks (such as (010) and (110)), were
323 identified as hydrocalumite ($Ca_4Al_2(OH)_{12}(Cl,CO_3,OH)2{\cdot}4H_2O$, PDF#16-0333 &
324 PDF#31-0245). In LDH_b, a slight shift towards larger d-value indicated the
325 overlapping of reflections from hydrocalumite (002) and hydrotalcite
326 ($Mg_6Al_2(OH)_{16}CO_3{\cdot}4H_2O$, PDF#42-2428) (003). The intensity of the reflection
327 (e.g., d_{003}), serving as a measure of crystallinity, revealed that LDH displayed
328 high crystallinity. Moreover, the d_{003} reflection intensity in LDH_a was
329 considerably lower than in LDH_b, suggesting that the introduction of Mg resulted
330 in a more ordered crystal lattice structure and may form tighter chemical bonds
331 with Ca, Al, and interlayer anions, thereby further stabilizing the crystal structure
332 (Takaki et al., 2016; Jiang et al., 2019; Zhang et al., 2020b). Furthermore, the
333 presence of only a few weak intensity impurity reflections in the XRD patterns
334 of LDH confirmed the relatively high purity of the environmentally friendly
335 synthesized products, with minimal impurities present.
336

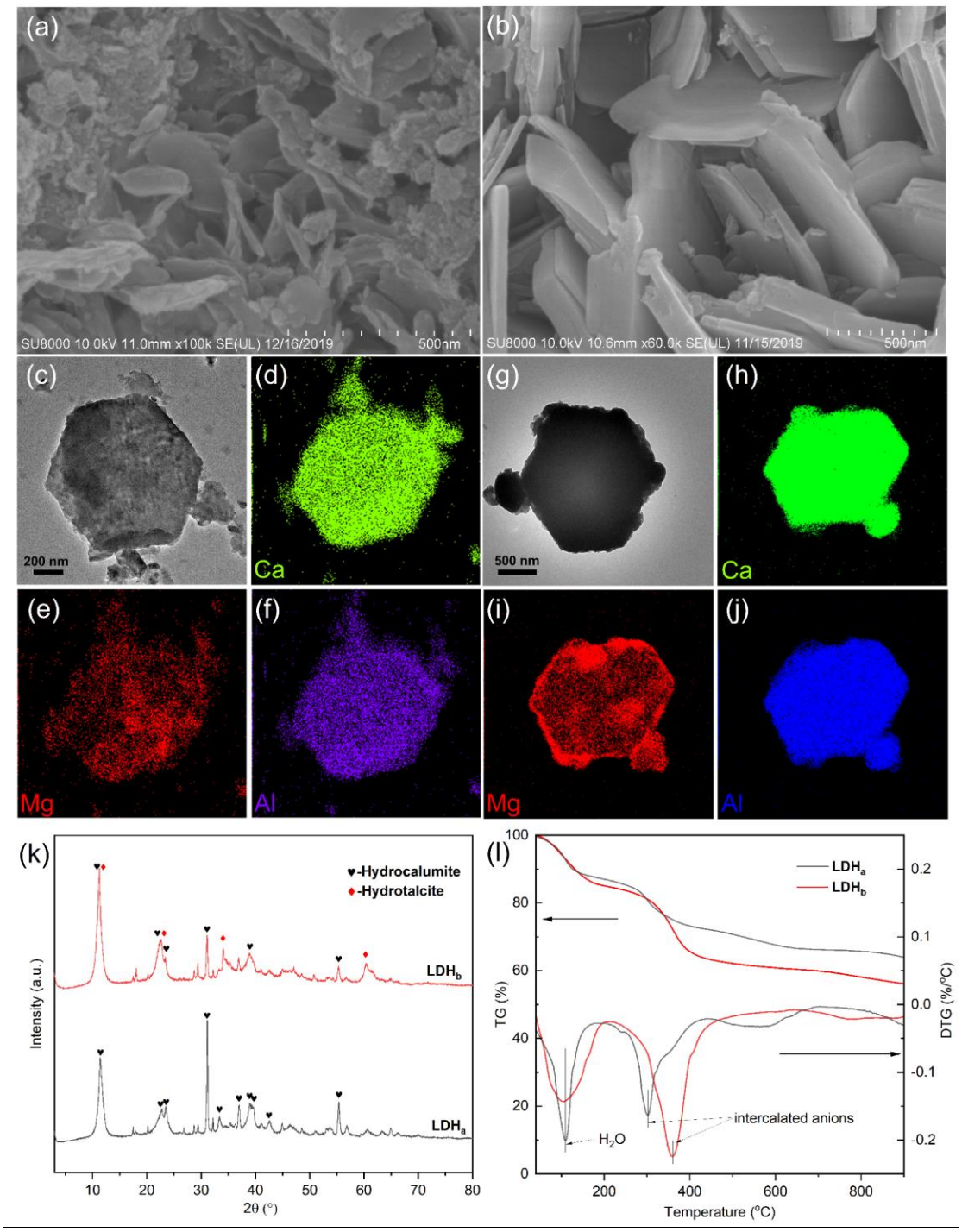

337

338 **Fig. 2.** (a), (b) Surface morphology of LDH_a, LDH_b; (c-j) TEM image and

339 elemental distribution of LDH_a, LDH_b; (k) crystal structure, and (l) thermal

340 characteristics of the green synthesized LDH.

341

342 Thermogravimetric analysis (TGA) experiments were carried out to investigate

343 the thermal characteristics of the synthesized LDH. The TG and the first
344 derivative of TG (DTG) curves of the samples are shown in Fig. 2l. Two distinct
345 mass loss peaks are evident on the DTG curves. The first peak is observed at
346 approximately 105°C, with LDH_a and LDH_b experiencing mass losses of 12.6%
347 and 15.3%, respectively. These losses are attributed to the evaporation of free
348 water molecules from the surface and interlayers of LDH materials (Chen et al.,
349 2018; Bukhtiyarova, 2019). The second intense and sharp peak, centered
350 between 300°C and 400°C, is ascribed to the decomposition of intercalated
351 anions (including CO_3^{2-}, OH^- and Cl^-) (Kuwahara et al., 2010; Gabriella
352 Alexandre Borgesa et al., 2020), resulting in mass losses of 15.2% and 23.3%
353 for LDH_a and LDH_b, respectively. The intensities of mass loss peaks associated
354 with intercalated anions are strengthened with the addition of MgO, suggesting
355 the formation of covalent bonds between the heavier intercalated anions and
356 metal ions in the layer structure (Yang et al., 2020). However, further
357 spectroscopic evidence is needed to validate this hypothesis. Additionally, the
358 second peak shifts to higher temperatures upon the incorporation of MgO in the
359 raw materials, indicating an enhancement in the thermal stability of the product,
360 which is consistent with the findings obtained from the X-ray diffraction (XRD)
361 analysis of LDH.
362
363 To discern the structural modifications induced by the green synthesis process
364 in GGBS, we conducted further investigations on the structures of both GGBS

365 and LDH using FTIR and XPS. FTIR analysis was employed to investigate the
366 vibrational characteristics of the octahedral lattice, hydroxyl groups, and
367 interlayer anions in the synthesized LDH (Fig. 3). The observed broad bands
368 around 3480 cm^{-1} were attributed to the hydrogen bonding stretching vibration
369 of hydroxyl groups in the interlayer water molecules of LDH (Cavani et al., 1991).
370 Additionally, the band at approximately 1630 cm^{-1} indicated the O-H bending
371 vibration of the interlayer water (δH-O-H) molecules of LDH (Elhalil et al., 2018).
372 In all spectra, the bands at about 1440 cm^{-1} and 874 cm^{-1} were identified as the
373 v_3 and v_2 vibrations of interlayer carbonate ions (Wang et al., 2013), implying
374 the capture of a small amount of carbon dioxide from the air by LDH. Notably,
375 the carbonate ion bands in LDH_b's spectrum were more pronounced than in
376 LDH_a, consistent with LDH_b's higher mass loss due to interlayer ion
377 decomposition. In the low-frequency region, adsorption bands at approximately
378 793 cm^{-1} and 422 cm^{-1} were observed, attributed to the M-O (M = Ca, Mg, or
379 Al) lattice vibrations (Goh et al., 2009; Zhou et al., 2018). Furthermore, LDH'
380 spectra exhibited bending vibrations of M-OH at approximately 540 cm^{-1}, 581
381 cm^{-1}, and 1040 cm^{-1} (Huang et al., 2014; Zhang et al., 2020b). A comparison
382 with the FTIR spectrum of GGBS (Fig. S3) revealed the disappearance of
383 functional groups at around 964 cm^{-1} (Si/Al-O) and 702 cm^{-1} (Si-O-Si/Al) in the
384 starting materials, confirming the removal of Si and the formation of a new
385 structure (El Didamony et al., 2012; Adeniyi and Ogundiran, 2020).

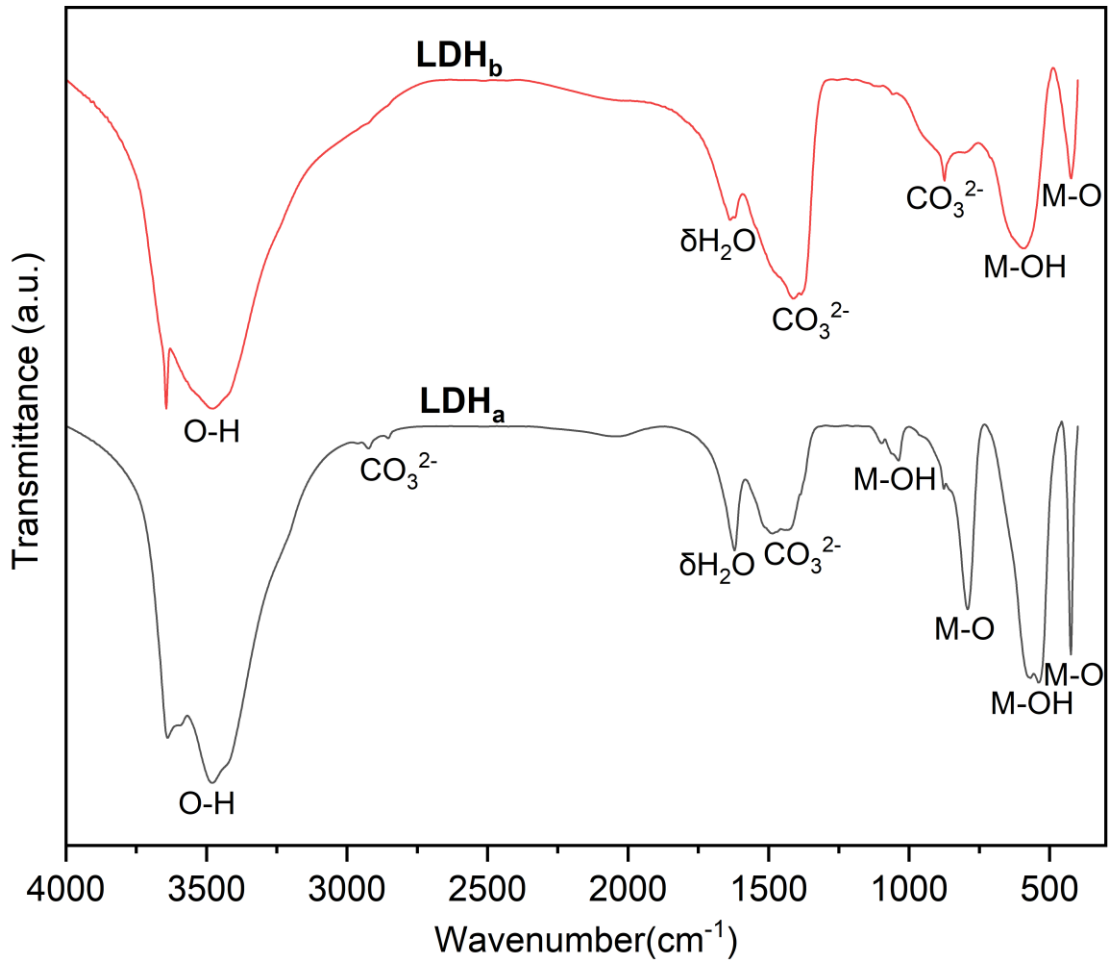

386

387 **Fig. 3.** Surface functionality of green synthesized LDH as revealed by FTIR.

388

389 The XPS analysis of LDH, as depicted in Fig. 4a, reveals prominent peaks
390 corresponding to Mg 1s, O 1s, Ca 2p, C 1s, Cl 2p, and Al 2p, indicating the
391 predominant presence of O, C, Ca, Mg, and Al in LDH. When compared to the
392 spectrum shown in Fig. S5a, the Si 2p peak in GGBS disappeared, while a new
393 Cl 2p peak emerged, signifying Si removal and chloride ion intercalation during
394 LDH synthesis (Dora et al., 2020). Upon scrutinizing the high-resolution XPS
395 spectra, distinct variations were observed in the Mg 1s and Al 2p peaks of LDH
396 compared to GGBS. While the Mg 1s peak in GGBS was observed at 1304.30

eV and the Al 2p peak at 74.20 eV (Fig. S5b, c), in LDH, these peaks shifted to lower binding energies, specifically 1303.87 eV and 1303.62 eV for Mg 1s, and 73.92 eV and 74.02 eV for Al 2p (Fig. 4b, c). This shifting pattern signifies the conversion of Mg and Al from the oxide structure in GGBS to the hydroxide structure in LDH layers (Chubar et al., 2013; Ye et al., 2016; Zhang et al., 2022a).

LDH_a displays Ca 2p doublet peaks at 350.97 eV and 347.02 eV, while LDH_b exhibits Ca 2p doublet peaks at 351.71 eV and 347.62 eV, corresponding to carbonate and hydroxide compounds of Ca, respectively (Matsushit et al., 1993; Zhang et al., 2022a). The observed increase in characteristic $CaCO_3$ peaks and decrease in $Ca(OH)_2$ peaks in Fig. 4d after MgO addition supports the earlier findings. Furthermore, a comparison of Al 2p and Ca 2p characteristic peak positions in LDH_a and LDH_b reveals a leftward shift in LDH_b, indicating an increase in binding energy and enhanced stability of the respective compounds (Cai et al., 2023).

The high-resolution C 1s spectrum (Fig. 4e) can be resolved into three components at approximately 289, 286, and 284.5 eV, attributed to carboxylate carbon (O-C=O) or carbonyl carbon (C=O), non-oxygenated cyclic carbon (C-C), and carbon in C-O, respectively (Goh et al., 2009; Huang et al., 2021). Unlike the material derived from pure GGBS, the MgO-doped sample exhibited a dominant oxygen-containing functional group, namely O-C=O, instead of C-

O, with its characteristic peak shifting to higher binding energy due to the presence of CO_3^{2-} in the interlayer (Zou et al., 2016). The high-resolution O 1s spectrum (Fig. 4f) can be deconvoluted into four components around 532.8, 531.7, 531.2, and 530.5 eV, representing C=O, H-O-H, M-OH, and M-O-M groups, respectively (Goh et al., 2009; Ravuru et al., 2021). The corresponding high-resolution spectrum of GGBS in Fig. S5f exhibits characteristic peaks at 532.45, 531.65, 531.40, and 530.55 eV, corresponding to Si-O-Si, C=O, Al-O/M-OH, and M-O-M groups (Dora et al., 2020). Based on the above analysis, it can be concluded that the treatment of GGBS resulted in the cleavage of Si-O-Si bonds, leading to the dissolution and subsequent removal of a significant amount of Si. The remaining alkali earth metals (Ca, Mg, Al) reacted with O to form new functional groups such as H-O-H, M-OH, and M-O-M in the interlayer.

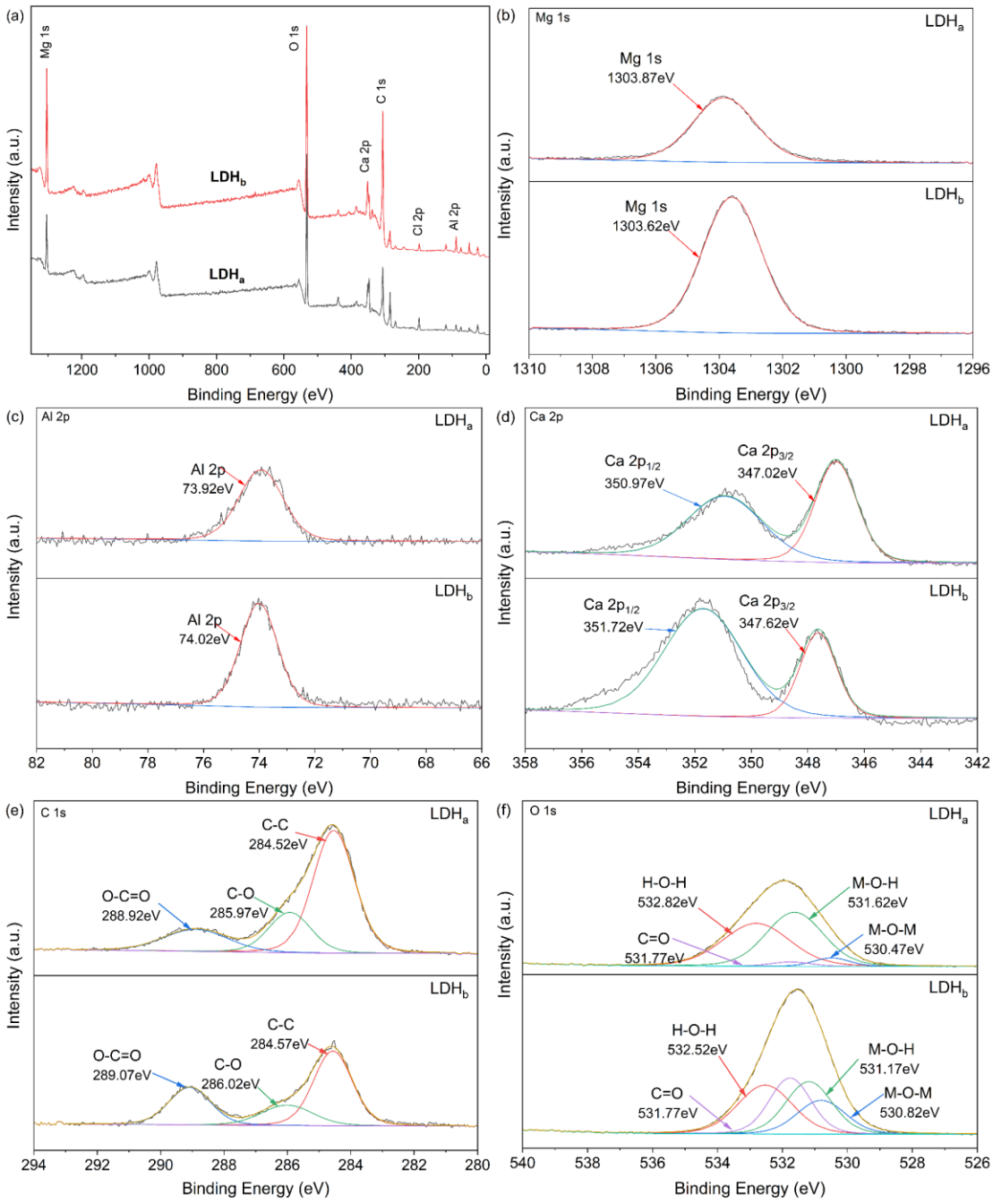

Fig. 4. (a) XPS survey spectra of LDH. (b) Mg 1s, (c) Al 2p, (d) Ca 2p, (e) C 1s and (f) O1s spectra of LDH. All spectrograms are drawn based on the premise of C correction.

3.2 Adsorption performances

Batch experiments were undertaken to investigate the impact of initial solution pH on the removal efficiency of Cd(II) and As(V) by LDH_a and LDH_b materials. Fig. 5a and b demonstrate that both LDH_a and LDH_b exhibited near-total dissolution under the initial pH of 2. At pH 3, 91.5% of Ca ions were leached from LDH_a, and even with subsequent pH increase, the leaching of Ca remained notably high, whereas the leaching of Al gradually increased, and a significant portion of Mg ions remained in the solid phase. This phenomenon is likely attributed to Cd displacing Ca under low pH conditions and solid-phase transformation at higher pH levels (Shan et al., 2015). When the initial pH of the solution was adjusted to 4 or higher, the solution's pH after LDH_a adsorption substantially increased to above 10.2, resulting in the almost complete removal of Cd(II) from the aqueous phase (Fig. 5a, b). At initial pH values ranging from 2 to 12, LDH_a exhibited As(V) removal efficiencies between 75.5% and 97.3%, while LDH_b displayed removal efficiencies between 89.3% and 98.6% (Fig. 5c, d). Overall, LDH_b exhibited superior adsorption performance for As(V) across different initial solution pH conditions. Monitoring of ion intensity and pH in the solution after reaching adsorption equilibrium revealed that LDH_b had a lower leaching rate of Al ions compared to LDH_a, and the adsorption process caused an increase in solution pH. This effect can be attributed to the release of OH^- and CO_3^{2-} from the interlayer of LDH during the adsorption process (Cavani et al., 1991).

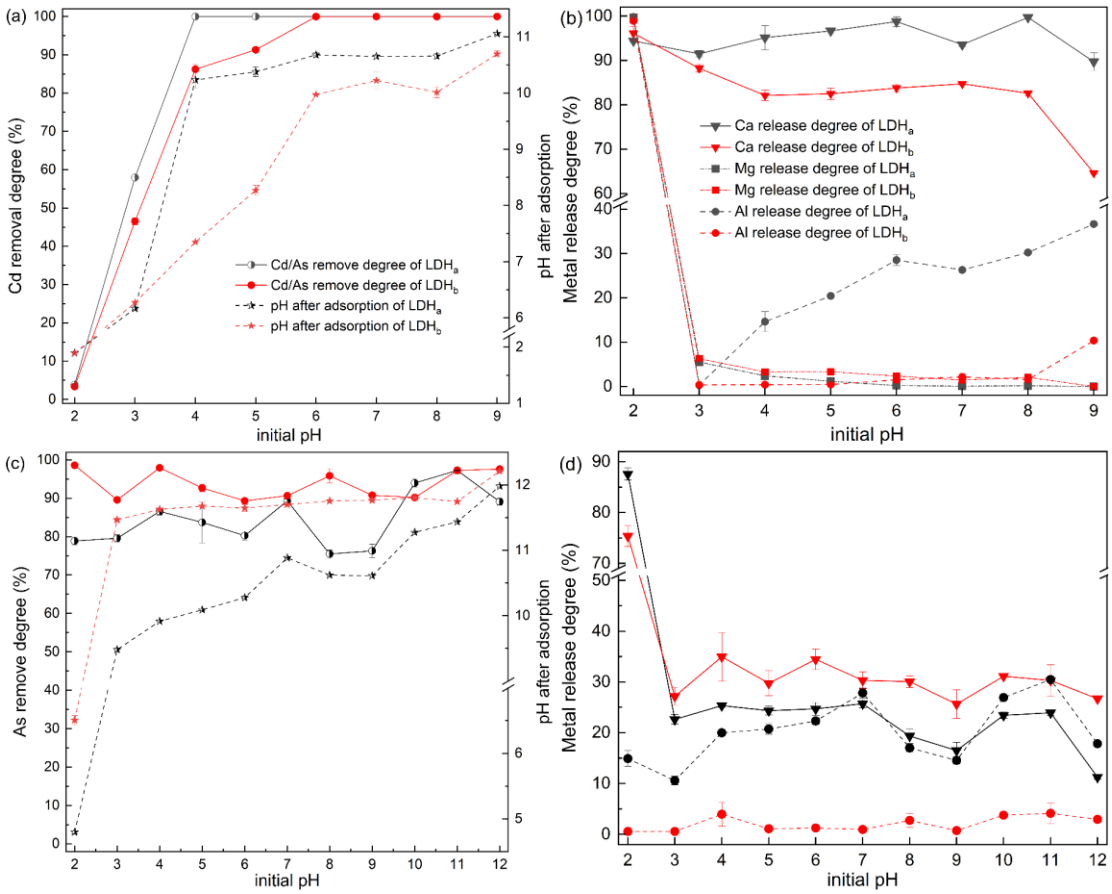

Fig. 5. (a), (b) Effect of pH on Cd(II) adsorption and element release, (c), (d) effect of pH on As(V) adsorption and element release.

The adsorption isotherms of Cd(II) and As(V) at 298K are presented in Fig. 6a and c, respectively. Table S5 provides the relevant parameters and correlation coefficients for the Langmuir and Freundlich models. The Langmuir model (R^2 of 0.895 and 0.977) better described the experimental data for Cd(II) adsorption on LDH indicating monolayer coverage on the homogeneous surface sites of these materials during adsorption (Wang et al., 2020b). On the other hand, the adsorption data of As(V) on LDH were better fitted with the Freundlich model

(R^2 of 0.950 and 0.913), suggesting a more complex heterogeneous surface adsorption process (Lu et al., 2018). The maximum adsorption capacities (Q^o_{max}) of As(V) by LDH_a and LDH_b were 104 and 126 mg/g, respectively, while the maximum adsorption capacities of Cd(II) for LDH_a and LDH_b were 567 and 422 mg/g, respectively. In comparison to various types of LDH synthesized using purified chemical reagents, green-synthesized LDH exhibits outstanding adsorption capabilities, particularly in the removal of Cd(II) from aqueous solutions (Table S7).

Fig. 6b and d displays the adsorption of Cd(II) and As(V) in aqueous solutions over time, and the corresponding model fitting parameters of PFO (Pseudo First Order), PSO (Pseudo Second Order), and Elovich are summarized in Table S6. At an initial Cd(II) concentration of 100 mg/L, as depicted in Fig. 6(a), LDH_a removed 92.2% of Cd(II) within 1 h, achieving >99% removal at equilibrium in less than 3 h. In comparison, LDH_b removed 81.1% of total Cd(II) within 1 h, and it took approximately 24 h to reach equilibrium with over 90% Cd removal. The kinetic data of Cd(II) adsorption demonstrated a good fit to the PSO model. As for As(V) adsorption, as shown in Fig. 6(d), LDH_a and LDH_b immobilized 28.6% and 62.0% of the total As(V), respectively, with both materials requiring 48 h to reach equilibrium and achieving an As(V) removal rate of approximately 99%. Generally, the PSO model provided a better fit to the kinetic data compared to other models, with R^2 values of 0.972 and 0.950. The calculated k_2 values from the PSO model followed the order LDH_b > LDH_a.

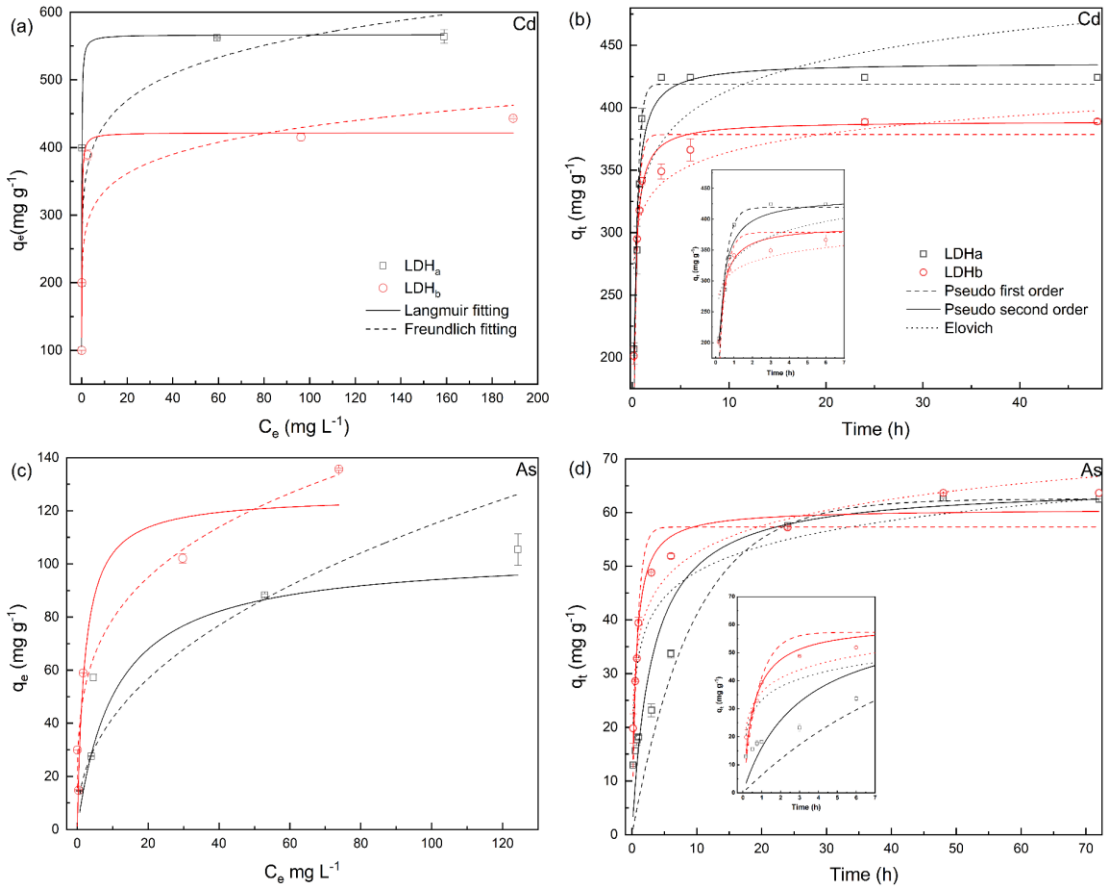

Fig. 6. (a) Cd(II) adsorption isotherm, (b) Cd(II) adsorption kinetics, (c) As(V) adsorption isotherm, and (d) As(V) adsorption kinetics of LDH. Modeling parameters are provided in Table S5 and Table S6.

3.3 Immobilization performances

Emboldened by the remarkable performance demonstrated in removing Cd(II) and As(V) ions from solution, the green-synthesized LDH were pursued as promising candidates for the remediation of Cd and As-contaminated soils. Stabilization experiments were conducted using contaminated farmland soil collected from Southwest China, and contaminated soil from an ore processing

503 site in Southwest China. After the addition of LDH, both types of soils exhibited
504 an increase in soil pH. Moreover, as the dosage of LDH increased, the soil pH
505 showed a gradual rise, a phenomenon known as the liming effect (**Error!**
506 **Reference source not found.**a, b) (Wang et al., 2023b; Yu et al., 2023). This
507 pH increase can be attributed to the gradual dissolution of hydroxyl groups and
508 alkali metal ions from LDH during the immobilization process (Zhang et al.,
509 2022b). The rise in soil pH contributes to the reduction of metal mobility, as the
510 increased negative surface charges enhance the adsorption of metal cations
511 by soil particles and promote metal precipitation (Yi et al., 2017). However, the
512 pH-induced immobilization effect, referred to as the liming effect, is not stable
513 in the long term due to the absence of chemical bond formation (Wang et al.,
514 2020a). In comparison to LDH_b, LDH_a led to a more noticeable increase in soil
515 pH in the initial days after application, but this was followed by a more significant
516 decrease (Fig. 7a, b). By the 14th day, the soil pH of the LDH_a-treated soil at
517 the same dosage was lower than that of the LDH_b-treated soil. This finding is
518 consistent with the earlier analysis, indicating that LDH_a exhibits higher activity
519 and reacts more rapidly in the soil environment.
520

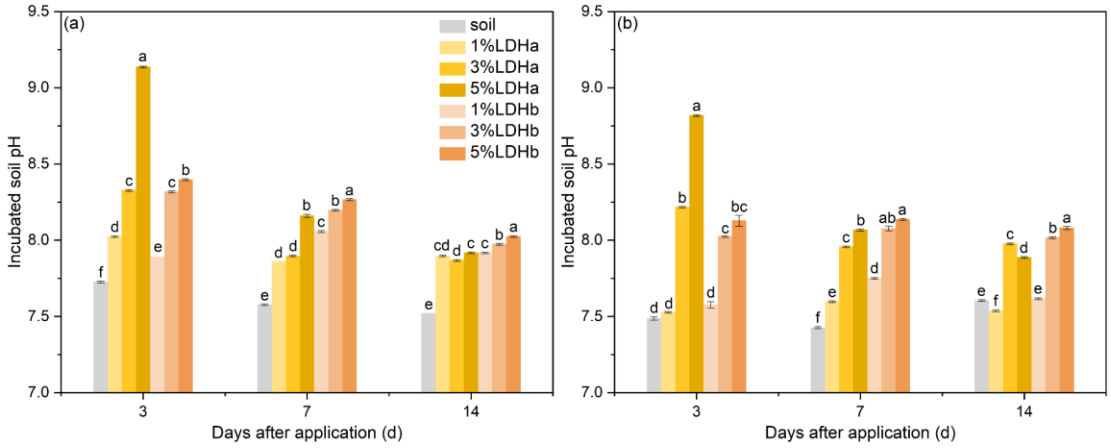

521

522 **Fig. 7.** Changes in soil pH following LDH amendment. (a) amended

523 agricultural soil; (b) amended industrial site soil.

524

525 The immobilization effects of LDH on Cd and As in soil contaminated with these

526 metals were assessed using the water extraction method and TCLP.

527 Additionally, the impact of LDH on the bioavailability of Cd and As in the

528 contaminated soil was evaluated using the DTPA extraction method. This

529 method, commonly employed in soil research, allowed for the evaluation of

530 extractable concentrations of Cd and As ions, which were found to be directly

531 proportional to the availability of these elements to plants in the soil (Dai et al.,

532 2004; Reyhanitabar and Gilkes, 2010; Zhao et al., 2022). The immobilization

533 performance of LDH in two different types of contaminated soils was found to

534 be limited under water leaching conditions, and in some cases, it even exhibited

535 activation of Cd in the soil. However, at higher LDH dosages, a significant

536 reduction in the leaching of bioavailable Cd was observed in the amended soils

537 compared to the unamended soils (Fig. 8 and Fig. 9). For instance, after 3 days

538 of remediation with 5% LDH_a, the bioavailable Cd in the contaminated farmland

539 soil decreased by 37.2%, while the group with 5% LDH_b showed a reduction of
540 24.1%. Considering that water leaching only accounts for a small fraction of
541 bioavailable Cd, the immobilization effect of LDH on Cd was demonstrated to
542 be present. As shown in Fig. 8e and Fig. 9e, the remediation effects of 3% and
543 5% LDH_a on both the contaminated farmland soil and industrial site soil were
544 evident after three days of treatment, but the immobilization effect decreased
545 slightly after seven days and became ineffective by day 14. Encouragingly, for
546 the farmland soil treated with 5% LDH_b, although there was a decline in
547 immobilization effect, the BDR remained stable, being 17.3% on day 7 and 16.6%
548 on day 14. The industrial site soil exhibited a similar trend, attributed to the
549 greater stability of LDH_b compared to LDH_a (section 3.1). The results of the
550 TCLP leaching experiments (Fig. 8c and Fig. 9c) indicated a significant
551 reduction in the concentration of leached Cd in the farmland soil remediated
552 with LDH at higher addition rates. The immobilization performance of LDH_b was
553 superior to LDH_a, and the stabilization effect increased gradually during the
554 short-term immobilization process. For example, on day 14, the IR of Cd (25.9%)
555 was higher than on day 3 (19.6%), similar to the results obtained with other
556 types of remediation agents for stabilizing heavy metal-contaminated soils in
557 TCLP experiments. This finding suggests that the immobilization of Cd by LDH
558 is a gradually evolving process (Wang et al., 2020a; Wang et al., 2022a).
559 Furthermore, LDH_a did not exhibit a stabilization effect in the industrial site soil,
560 while LDH_b showed an IR of 9.75-11.6% at 5% addition rate.

A discernible pattern is observed in the concentration of bioavailable Cd in the soil and soil pH (Fig. 7). After a 3-day incubation, the pH of the amended soil increases with the dosage of LDH, concurrently enhancing the remediation effect on bioavailable Cd in soil. Due to its higher reactivity, LDH_a caused a rapid increase in soil pH upon amendment, exhibiting a significant Cd stabilization effect (BDR reaching 37.2% and 29.8% at a 5% dosage for agricultural and industrial soils, respectively). However, with the increasing incubation time, the soil underwent a pH decline which gradually led to a weakening of the Cd immobilization effect. In contrast, soils treated with LDH_b showed only a marginal decline in pH over time, possibly attributed to a more robust liming effect. Concurrently, the bioavailable Cd concentration remained relatively stable. At a 5% dosage, the bioavailable Cd concentrations in agricultural and field soils on days 3, 7, and 14 are 3.42, 3.44, 3.40 mg/kg, and 2.06, 2.02, 1.96 mg/kg, respectively. Previous studies indicate that the elevation of pH following soil amendment is a primary mechanism for immobilizing cationic metals in soil (Yang et al., 2022; Guo et al., 2023; Zong et al., 2023). For instance, the study by Lyu et al. (2023) used CaMgAl-LDH for the remediation of soil contaminated with Cd, and Pb, which found a significant negative correlation ($P < 0.05$) between pH and the extractable content of Cd and Pb. The study by Zhang et al. (2022a) explored the immobilizaiton mechanisms of CaAl-LDH and MgAl-LDH toward Cd immobilization in a

polluted soil, which observed that soil pH increased after LDH treatment, leading to the precipitation of exchangeable Cd into $CdCO_3$(s) in soil. In this study, the increase in soil pH induced by the addition of LDH likely represents the primary stabilization mechanism toward Cd.

The immobilization performance of LDH on As in contaminated soil was more pronounced, in contrast to their performance on Cd in contaminated soil. As shown in Fig. 8 b, d, f and Fig. 9 b, d, f, the stabilization effect of LDH exhibited consistent variations with different raw material ratios, dosages, and modification durations in both types of soil. Overall, with an increase in dosage, LDH demonstrated a significant enhancement in immobilizing As. For instance, at 1%, 3%, and 5% dosage, LDH_a achieved 55.4%, 76.3%, and 83.8% BDR (bioavailable As) in the farmland soil on the 14th day after application. Importantly, under neutral environmental conditions (water extraction and DTPA extraction), LDH_a exhibited a significantly superior As immobilization performance compared to LDH_b, which was quite different from LDH' adsorption behavior towards As in water. This may be attributed to the differences in the chemical properties and reaction mechanisms of LDH under different environmental conditions. In water, the chemical reaction rate is faster, and the adsorption process is mainly controlled by surface adsorption (Shen et al., 2019; Zhang et al., 2020a). LDH_b exhibited strong adsorption capabilities of As in water, which was primarily attributed to the provision of active hydroxyl for the

605 complexation of As anions (Section 3.2) (Nguyen et al., 2022; Shao et al., 2023).
606 However, during As immobilization in soil, besides the aqueous-phase
607 adsorption, As also interacts with oxides and organic matter on the soil particle
608 surfaces, forming stable complexes or precipitates. Additionally, after LDH are
609 added to the soil, the porous structure is disrupted, promoting stronger
610 interaction of LDH_a with other components in the soil and inducing more efficient
611 immobilization reactions on the soil particle surfaces (Wang et al., 2020b; Wang
612 et al., 2022a). On the other hand, when the soil environment is under acidic
613 conditions (TCLP), the immobilization effects of both LDH_a and LDH_b are
614 roughly similar and significantly superior to those under neutral conditions. For
615 example, at 5% dosage, the IR of LDH_a and LDH_b after 14 days of water
616 extraction are 89.6% and 62.0%, respectively, while the BDR after DTPA
617 extraction are 83.8% and 54.8%, respectively, and both IR increase to 95.2%
618 and 95.4% after TCLP extraction.
619
620 Different from Cd immobilization which was predominantly driven by soil pH
621 variations, the immobilization efficacy of LDH_a for As did not fade with
622 decreasing pH over time. LDH_b demonstrated an enhanced immobilization
623 effect toward As as pH gradually decreases. For instance, the BDRs of As in
624 agricultural soil amended with LDH_b were 28.8%, 30.5%, and 39.5% on days 3,
625 7, and 14, respectively, at a 3% application dosage. This trend was also found
626 for a higher dosage of 5%. Numerous studies have confirmed that the addition

627 of alkaline stabilization agents will increase soil pH, thus increasing the surface
628 charge negativity of soil particles. This phenomenon will lead to the mobilization
629 of oxyanion As due to electrostatic repulsion (Bandara et al., 2020; Zhong et al.,
630 2021; Yang et al., 2022). Due to its positively charged cationic layered structure,
631 LDH exhibits the ability to impede further migration of As, even in scenarios
632 where soil pH increases, thereby reducing arsenic leaching. This is achieved
633 through electrostatic adsorption (Wang et al., 2018; Shuang Xu, 2020).
634 Additionally, previous research have frequently reported that interlayer ion
635 exchange is the primary mechanism by which LDH removes free As anions
636 (Huang et al., 2015; Liu et al., 2019). Besides, surface complexation reactions
637 also played a role in As immobilization. We found that LDH_a possessed more
638 hydroxyl functional groups on its surface and interlayers, while LDH_b had a
639 richer carbonate content (Section 3.1).
640
641 Table S8 provides a comprehensive overview of studies employing LDH as
642 amendments for immobilizing Cd or As in soil. The effectiveness of Cd
643 remediation in soils using LDH prepared through green synthesis method were
644 comparable or lower than LDH synthesized using purified chemical reagents. It
645 is important to highlight that the As remediation effectiveness of green-
646 synthesized LDH surpasses that reported in the majority of the literature.

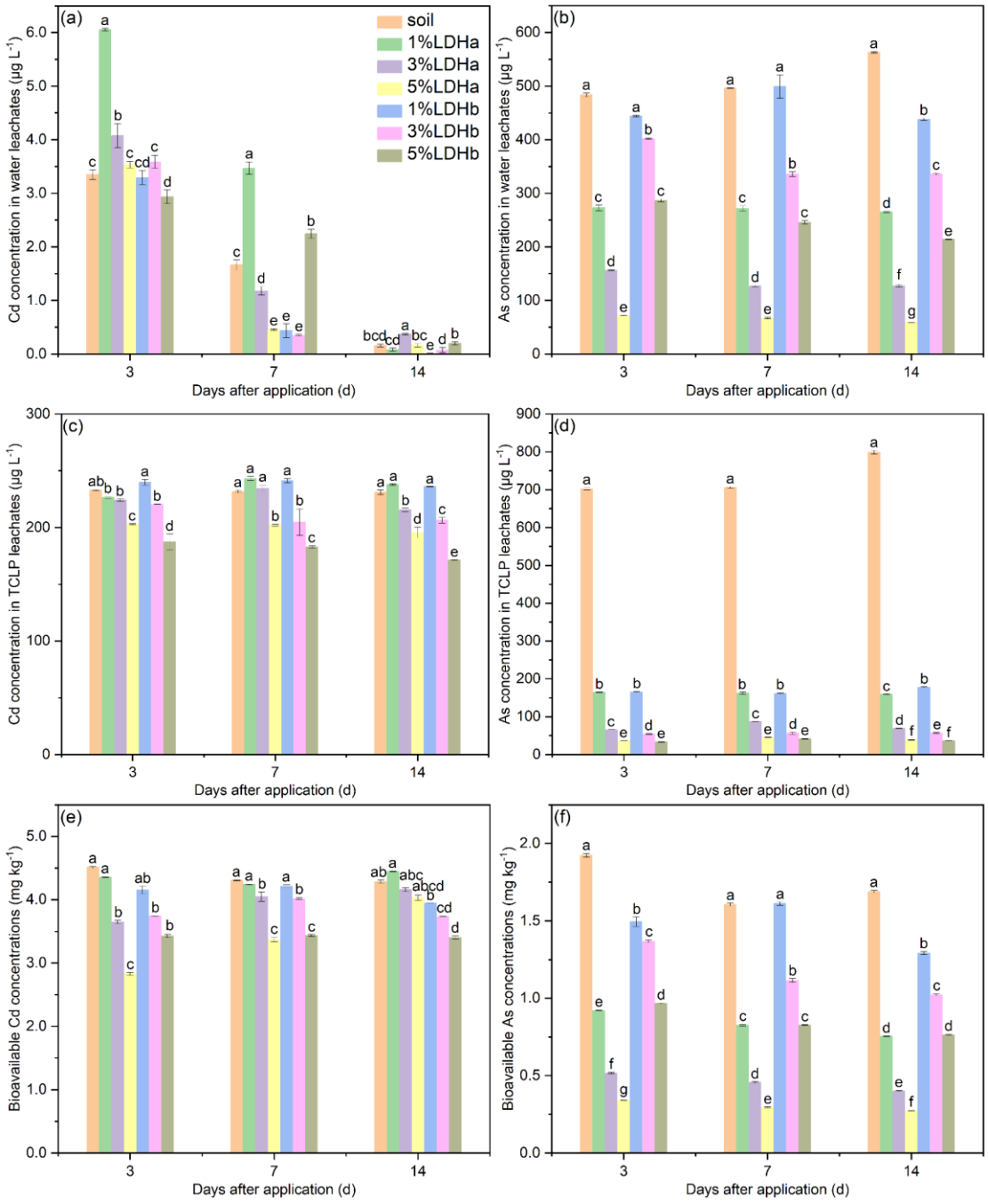

Fig. 8. (a) Cd, (b) As concentration in water leachates of agricultural soil following LDH amendment. (c) Cd, (d) As concentration in TCLP leachates of agricultural soil following LDH amendment. Bioavailable (e) Cd, (f) As concentrations of amended and unamended agricultural soil.

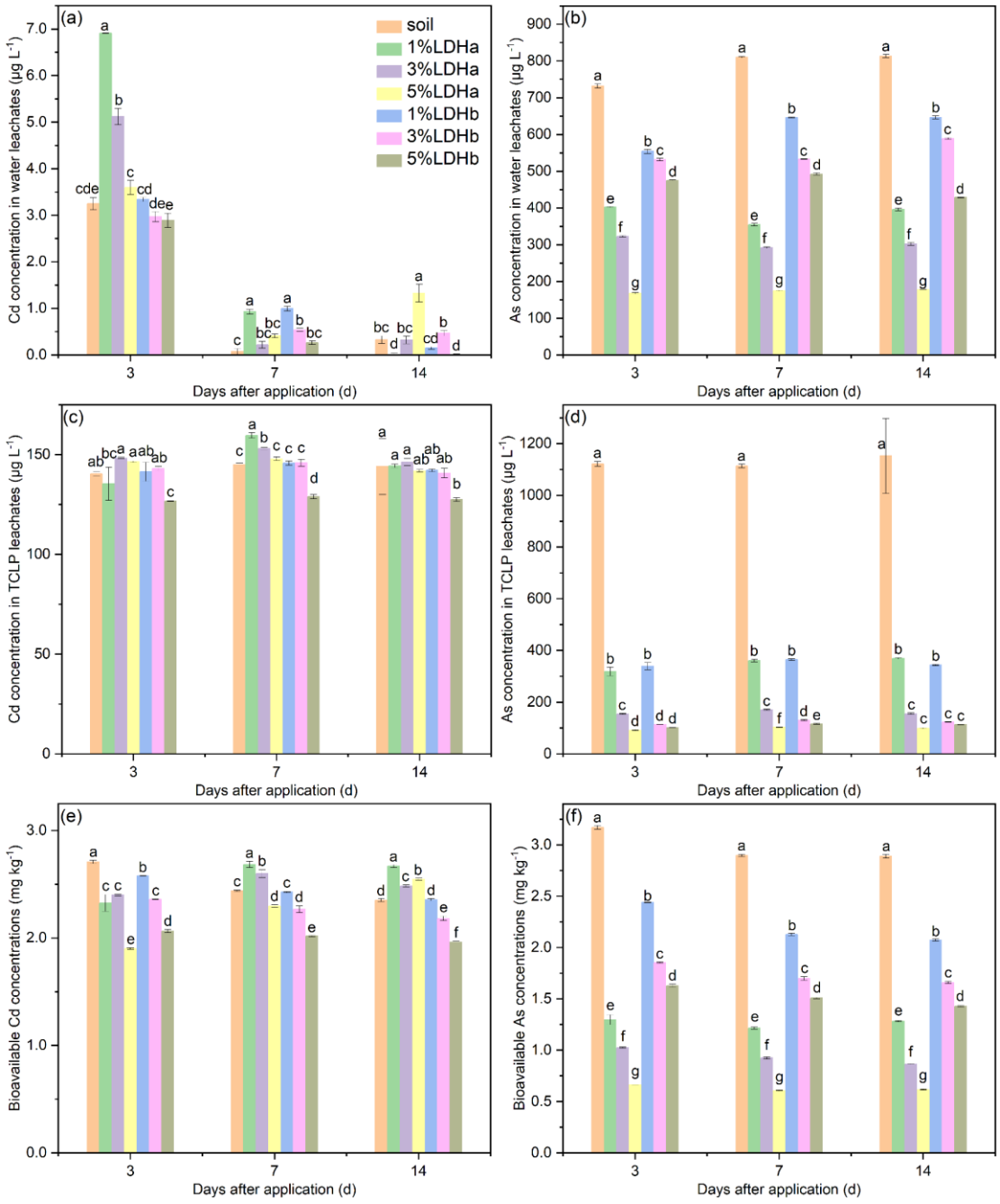

653

654 **Fig. 9.** (a) Cd, (b) As concentration in water leachates of industrial site soil

655 following LDH amendment. (c) Cd, (d) As concentration in TCLP leachates of

656 industrial site soil following LDH amendment. Bioavailable (e) Cd, (f) As

657 concentrations of amended and unamended industrial site soil.

658

4 Conclusions

In this study, a green synthesis method of layered double hydroxides (LDH) aimed for heavy metal adsorption was proposed, utilizing industrial waste GGBS from iron-making industry, and naturally abundant material MgO. The synthesized products with various raw material compositions were comprehensively characterized through a series of analytical techniques. The evidence showed that the addition of 20% MgO in the raw materials for LDH synthesis (LDH_b) improved its stability compared to LDH synthesized solely from pure GGBS (LDH_a). Batch adsorption experiments demonstrated the superior adsorption characteristics of the green-synthesized LDH towards As(V) and Cd(II). Experimental results on the stabilization of Cd and As in contaminated farmland and industrial site soils revealed that both materials exhibited a immobilization effect, making them promising green remediation materials for stabilizing soil heavy metals.

Acknowledgement

This work was supported by the Guangxi Key Research and Development Program (Grant No. GUIKE AB22035036), and the National Natural Science Foundation of China (Grant No. 42077118).

Declaration of competing interest

The authors declare that they have no known competing financial interests or personal relationships that could have appeared to influence the work reported in this paper.

Data availability

Data will be made available on request.

References

Adeniyi, F.I., Ogundiran, M.B., 2020. Synthesis of geopolymer binders and mortars from Ijero-Ekiti calcined clay, blast furnace slag and river sand. Earthline Journal of Chemical Sciences 4, 15-34.

Alothman, Z.A., 2012. A review: fundamental aspects of silicate mesoporous materials. Materials 5, 2874-2902.

Bandara, T., Franks, A., Xu, J., Bolan, N., Wang, H., Tang, C., 2020. Chemical and biological immobilization mechanisms of potentially toxic elements in biochar-amended soils. Critical Reviews in Environmental Science and Technology 50, 903-978.

Bellotto, M., Rebours, B., Clause, O., Lynch, J., Bazin, D., Elkaïm, E., 1996. A reexamination of hydrotalcite crystal chemistry. The Journal of Physical Chemistry 100, 8527-8534.

Bukhtiyarova, M.V., 2019. A review on effect of synthesis conditions on the formation of layered double hydroxides. Journal of Solid State Chemistry 269, 494-506.

Cai, H., Ma, K., Zhang, Y., Li, X., Wang, W., Tong, S., 2023. Carbonizing hollow metal–organic framework/layered double hydroxide (MOF/LDH) nanocomposite with excellent adsorption capacity for removal of Pb (II) and organic dyes from wastewater. Carbon Research 2, 23.

Cavani, F., Trifiro, F., Vaccari, A., 1991. Hydrotalcite-type anionic clays: preparation, properties and applications. Catal. Today 11, 173-301.

Chen, W.Q., Xing, J.L., Lu, Z.H., Wang, J., Yu, S.J., Yao, W., Asiri, A.M., Alamry, K.A., Wang, X.K., Wang, S.H., 2018. Citrate-modified Mg-Al layered double hydroxides for efficient removal of lead from water. Environ. Chem. Lett. 16,

561-567.
Chubar, N., Gerda, V., Megantari, O., Mičušík, M., Omastova, M., Heister, K., Man, P., Fraissard, J., 2013. Applications versus properties of Mg–Al layered double hydroxides provided by their syntheses methods: Alkoxide and alkoxide-free sol–gel syntheses and hydrothermal precipitation. Chem. Eng. J. 234, 284-299.
Dai, J., Becquer, T., Rouiller, J.H., Reversat, G., Bernhard-Reversat, F., Nahmani, J., Lavelle, P., 2004. Heavy metal accumulation by two earthworm species and its relationship to total and DTPA-extractable metals in soils. Soil Biology and Biochemistry 36, 91-98.
Dora, J.K., Nayak, D., Ghosh, S., Adyam, V., Yedla, N., Kundu, T.K., 2020. A facile and green synthesis approach to derive highly stable SiO x-hard carbon based nanocomposites for use as the anode in lithium-ion batteries. Sustainable Energy & Fuels 4, 6054-6065.
El Didamony, H., Assal, H., El Sokkary, T., Abdel Gawwad, H., 2012. Kinetics and physico-chemical properties of alkali activated blast-furnace slag/basalt pastes. HBRC Journal 8, 170-176.
Elhalil, A., Farnane, M., Machrouhi, A., Mahjoubi, F.Z., Elmoubarki, R., Tounsadi, H., Abdennouri, M., Barka, N., 2018. Effects of molar ratio and calcination temperature on the adsorption performance of Zn/Al layered double hydroxide nanoparticles in the removal of pharmaceutical pollutants. Journal of Science: Advanced Materials and Devices 3, 188-195.
Gabriella Alexandre Borgesa, Gabriel Max Dias Ferreirab, Kisla Prislen Félix Siqueirac, Anderson Diasa, Keirom Osmany Nàjera Navarrob, Silvia Juliana Barros e Silvab, Guilherme Dias Rodriguesa, Magesteb, A.B., 2020. Adsorption of organic and inorganic arsenic from aqueous solutions using MgAl-LDH with incorporated nitroprusside. J. Colloid Interface Sci. 575, 194-205.
Goh, K.-H., Lim, T.-T., Dong, Z., 2009. Enhanced Arsenic Removal by Hydrothermally Treated Nanocrystalline Mg/Al Layered Double Hydroxide with Nitrate Intercalation. Environmental Science & Technology 43, 2537-2543.
Guan, X., Yuan, X., Zhao, Y., Wang, H., Wang, H., Bai, J., Li, Y., 2022. Application of functionalized layered double hydroxides for heavy metal removal: A review. Sci. Total Environ. 838, 155693.
Guo, H., Jiang, H., Li, Y., Yan, B., Li, P., 2019. Evaluation of chromate removal using layered double hydroxides and their calcined products derived from blast furnace slag. Journal of Environmental Engineering 145, 04019051.
Guo, J., Wang, L., Qu, G., Liu, X., Lian, Y., Hou, D., 2023. Soil health improvement in a karst area with geogenic Cd enrichment using biochar and clay-based amendments. Journal of Soils and Sediments.
He, F., Chen, G., Yu, Y., Zhou, Y., Zheng, Y., Hao, S., 2015. The synthesis of condensed C-PDA–gC 3 N 4 composites with superior photocatalytic performance. Chemical Communications 51, 6824-6827.
Hou, D., 2021. Sustainable remediation in China: elimination, immobilization, or dilution. Environmental science & technology 55, 15572-15574.

Hou, D., 2022. Expediting climate‐smart soils management. Soil Use and Management 38, 1-6.
Hou, D., 2023. Sustainable soil management for food security. Wiley Online Library, pp. 1-7.
Hou, D., Al-Tabbaa, A., O'Connor, D., Hu, Q., Zhu, Y.-G., Wang, L., Kirkwood, N., Ok, Y.S., Tsang, D.C., Bolan, N.S., 2023. Sustainable remediation and redevelopment of brownfield sites. Nature Reviews Earth & Environment 4, 271-286.
Huang, L., Wang, J., Gao, Y., Qiao, Y., Zheng, Q., Guo, Z., Zhao, Y., O'Hare, D., Wang, Q., 2014. Synthesis of LiAl 2-layered double hydroxides for CO 2 capture over a wide temperature range. J. Mater. Chem. A 2, 18454-18462.
Huang, M., Lu, G., Pu, J., Qiang, Y., 2021. Superhydrophobic and smart MgAl-LDH anti-corrosion coating on AZ31 Mg surface. Journal of Industrial and Engineering Chemistry 103, 154-164.
Huang, P.P., Cao, C.Y., Wei, F., Sun, Y.B., Song, W.G., 2015. MgAl layered double hydroxides with chloride and carbonate ions as interlayer anions for removal of arsenic and fluoride ions in water. Rsc Advances 5, 10412-10417.
Hudcova, B., Vitkova, M., Ourednicek, P., Komarek, M., 2019. Stability and stabilizing efficiency of Mg-Fe layered double hydroxides and mixed oxides in aqueous solutions and soils with elevated As(V), Pb (II) and Zn(II) contents. Sci. Total Environ. 648, 1511-1519.
ISO, 2018. ISO 23470:2018: Soil quality — Determination of effective cation exchange capacity (CEC) and exchangeable cations using a hexamminecobalt(III)chloride solution. International Organization for Standardization.
IUPAC, 2015. Physisorption of gases, with special reference to the evaluation of surface area and pore size distribution (IUPAC Technical Report). International Union of Pure and Applied Chemistry 87, 1051-1069.
Jaworski, C.C., Krzywoszynska, A., Leake, J.R., Dicks, L.V., 2023. Sustainable soil management in the UK: a survey of current practices and how they relate to the principles of regenerative agriculture. Soil Use and Management.
Jiang, H., Guo, H., Li, P., Li, Y., Yan, B., 2019. Preparation of CaMgAl-LDHs and mesoporous silica sorbents derived from blast furnace slag for CO2 capture. Rsc Advances 9, 6054-6063.
Jin, Y., Wang, L., Song, Y., Zhu, J., Qin, M., Wu, L., Hu, P., Li, F., Fang, L., Chen, C., 2021. Integrated life cycle assessment for sustainable remediation of contaminated agricultural soil in China. Environmental Science & Technology 55, 12032-12042.
Jing, C., Liu, X., Liu, X., Jiang, D., Dong, B., Dong, F., Wang, J., Li, N., Lan, T., Zhang, Y., 2018. Crystal morphology evolution of Ni–Co layered double hydroxide nanostructure towards high-performance biotemplate asymmetric supercapacitors. CrystEngComm 20, 7428-7434.
Kuwahara, Y., Ohmichi, T., Kamegawa, T., Mori, K., Yamashita, H., 2010. A novel conversion process for waste slag: synthesis of a hydrotalcite-like

796 compound and zeolite from blast furnace slag and evaluation of adsorption
797 capacities. Journal of Materials Chemistry 20, 5052-5062.
798 Liang, X., Zang, Y., Xu, Y., Tan, X., Hou, W., Wang, L., Sun, Y., 2013. Sorption
799 of metal cations on layered double hydroxides. Colloids surfaces A:
800 physicochemical engineering aspects 433, 122-131.
801 Lide, D.R., 2004. CRC handbook of chemistry and physics. CRC press.
802 Lin, C., Luo, W., Luo, T., Zhou, Q., Li, H., Jing, L., 2018. A study on adsorption
803 of Cr (VI) by modified rice straw: Characteristics, performances and mechanism.
804 Journal of Cleaner Production 196, 626-634.
805 Liu, J., Wu, P., Li, S., Chen, M., Cai, W., Zou, D., Zhu, N., Dang, Z., 2019.
806 Synergistic deep removal of As (III) and Cd (II) by a calcined multifunctional
807 MgZnFe-CO3 layered double hydroxide: photooxidation, precipitation and
808 adsorption. Chemosphere 225, 115-125.
809 Lu, H., Liu, S., Zhang, H., Qiu, Y., Zhao, J., Zhu, Z., 2018. Decontamination of
810 arsenic in actual water samples by calcium containing layered double
811 hydroxides from a convenient synthesis method. Water 10, 1150.
812 Lyu, P., Li, L., Huang, X., Xie, J., Ye, J., Tian, Y., Huang, J., Zhu, C., 2023.
813 Ternary Ca–Mg–Al layered double-hydroxides for synergistic remediation of As,
814 Cd, and Pb from both contaminated soil and groundwater: Characteristics,
815 effectiveness, and immobilization mechanisms. Journal of Hazardous Materials
816 442, 130030.
817 Matsushit, I., Suzuki, T., Morig, T., Ashid, T., Nakabayash, I., Metso, J., 1993.
818 XPS study on the carbonation process of Ca (OH) 2. Journal of the Ceramic
819 Society of Japan 101, 725-727.
820 MEE, 2010. HJ557-2010: Solid waste-Extraction procedure for leaching
821 toxicity-Horizontal vibration method. Ministry of Ecology and Environment of the
822 People's Republic of China, Beijing, China.
823 MEE, 2016a. HJ 802-2016: Soil quality-Determination of conductivity-Electrode
824 method. Ministry of Ecology and Environment of the People's Republic of China,
825 Beijing, China.
826 MEE, 2016b. Soil-Determination of Bioavailable Form of Eight Elements-
827 Extraction with Buffered DTPA Solution/Inductively Couple Plasma Optical
828 Emission Spectrometry (HJ 804-2016). MEE (Ministry of Ecology and
829 Environment of the People’s Republic of China.
830 MEE, 2018. HJ 962-2018: Soil - Determination of pH - Potentiometry. Ministry
831 of Ecology and Environment of the People's Republic of China, Beijing, China.
832 Missau, J., Bertuol, D.A., Tanabe, E.H., 2021. Highly efficient adsorbent for
833 removal of Crystal Violet Dye from Aqueous Solution by CaAl/LDH supported
834 on Biochar. Applied Clay Science 214, 106297.
835 Newman, S.P., Jones, W., O'Connor, P., Stamires, D.N., 2002. Synthesis of the
836 3R 2 polytype of a hydrotalcite-like mineral. Journal of Materials Chemistry 12,
837 153-155.
838 Nguyen, T.H., Tran, H.N., Nguyen, T.V., Vigneswaran, S., Trinh, V.T., Nguyen,
839 T.D., Ha Nguyen, T.H., Mai, T.N., Chao, H.-P., 2022. Single-step removal of

arsenite ions from water through oxidation-coupled adsorption using Mn/Mg/Fe layered double hydroxide as catalyst and adsorbent. Chemosphere 295, 133370.
Peligro, F.R., Pavlovic, I., Rojas, R., Barriga, C., 2016. Removal of heavy metals from simulated wastewater by in situ formation of layered double hydroxides. Chem. Eng. J. 306, 1035-1040.
Ravuru, S.S., Jana, A., De, S., 2021. Performance modeling of layered double hydroxide incorporated mixed matrix beads for fluoride removal from contaminated groundwater with the scale up study. Separation and Purification Technology 277, 119631.
Reyhanitabar, A., Gilkes, R., 2010. Kinetics of DTPA extraction of zinc from calcareous soils. Geoderma 154, 289-293.
Rojas, R., 2014. Copper, lead and cadmium removal by Ca Al layered double hydroxides. Applied Clay Science 87, 254-259.
Shan, R.R., Yan, L.G., Yang, K., Hao, Y.F., Du, B., 2015. Adsorption of Cd(II) by Mg-Al-CO3- and magnetic Fe3O4/Mg-Al-CO3-layered double hydroxides: Kinetic, isothermal, thermodynamic and mechanistic studies. Journal of Hazardous Materials 299, 42-49.
Shao, P., Yin, H., Li, Y., Cai, Y., Yan, C., Yuan, Y., Dang, Z., 2023. Remediation of Cu and As contaminated water and soil utilizing biochar supported layered double hydroxide: Mechanisms and soil environment altering. Journal of Environmental Sciences 126, 275-286.
Shen, Z., Hou, D., Jin, F., Shi, J., Fan, X., Tsang, D.C., Alessi, D.S.J.S.o.t.T.E., 2019. Effect of production temperature on lead removal mechanisms by rice straw biochars. 655, 751-758.
Shen, Z., Zhang, Y., Hou, D., 2020. Layered double hydroxides for soil and groundwater remediation, Soil and Groundwater Remediation Technologies. CRC Press, pp. 147-164.
Shuang Xu, L.Z., Jiawen Zhao, Jing Cheng, Qianqian Yu, Shuwang Zhang, Jialing Zhao, Xinhong Qiu, 2020. Remediation of chromium-contaminated soil using delaminated layered double hydroxides with different divalent metals. Chemosphere.
Siddique, R., Iqbal Khan, M., 2011. Ground Granulated Blast Furnace Slag, in: Siddique, R., Khan, M.I. (Eds.), Supplementary Cementing Materials. Springer Berlin Heidelberg, Berlin, Heidelberg, pp. 121-173.
Smedley, P.L., Kinniburgh, D.G., 2002. A review of the source, behaviour and distribution of arsenic in natural waters. Appl. Geochem. 17, 517-568.
Sun, M., Xiao, Y., Zhang, L., Gao, X., Yan, W., Wang, D., Su, J.J.C.E.J., 2015. High uptake of Cu2+, Zn2+ or Ni2+ on calcined MgAl hydroxides from aqueous solutions: changing adsorbent structures. 272, 17-27.
Takaki, Y., Qiu, X., Hirajima, T., Sasaki, K., 2016. Removal mechanism of arsenate by bimetallic and trimetallic hydrocalumites depending on arsenate concentration. Applied Clay Science 134, 26-33.
Tran, H.N., Lin, C.C., Woo, S.H., Chao, H.P., 2018. Efficient removal of copper

and lead by Mg/Al layered double hydroxides intercalated with organic acid anions: Adsorption kinetics, isotherms, and thermodynamics. Applied Clay Science 154, 17-27.
US EPA, E., 1992. Method 1311: Toxicity characteristic leaching procedure.
USEPA, 2007. Method 3051A: Microwave Assisted Acid Digestion of Sediments, Sludges, Soils, and Oils. United States Environmental Protection Agency.
Vollpracht, A., Soutsos, M., Kanavaris, F., 2018. Strength development of GGBS and fly ash concretes and applicability of fib model code's maturity function–A critical review. Construction and Building Materials 162, 830-846.
Wang, H., Wang, L., Yang, B., Li, X., Hou, R., Hu, Z., Hou, D., 2023a. Sustainable soil remediation using mineral and hydrogel: field evidence for metalloid immobilization and soil health improvement. Journal of Soils and Sediments, 1-11.
Wang, J., Zhang, T., Li, M., Yang, Y., Lu, P., Ning, P., Wang, Q., 2018. Arsenic removal from water/wastewater using layered double hydroxide derived adsorbents, a critical review. RSC Advances 8, 22694-22709.
Wang, L., Bolan, N.S., Tsang, D.C., Hou, D., 2020a. Green immobilization of toxic metals using alkaline enhanced rice husk biochar: Effects of pyrolysis temperature and KOH concentration. Sci. Total Environ., 137584.
Wang, L., Hu, Z., Yin, H., Bradford, S.A., Luo, J., Hou, D., 2023b. Aging of colloidal contaminants and pathogens in the soil environment: Implications for nanoplastic and COVID‐19 risk mitigation. Soil Use and Management 39, 70-91.
Wang, L., Huang, J., Li, G., Luo, J., Bolan, N.S., Hou, D., 2022a. Long-term immobilization of soil metalloids under simulated aging: Experimental and modeling approach. Sci. Total Environ. 806, 150501.
Wang, L., Li, X., Tsang, D.C., Jin, F., Hou, D., 2020b. Green remediation of Cd and Hg contaminated soil using humic acid modified montmorillonite: immobilization performance under accelerated ageing conditions. Journal of Hazardous Materials, 122005.
Wang, L., Ok, Y.S., Tsang, D.C., Alessi, D.S., Rinklebe, J., Mašek, O., Bolan, N.S., Hou, D., 2022b. Biochar composites: Emerging trends, field successes and sustainability implications. Soil Use and Management 38, 14-38.
Wang, L., Rinklebe, J., Tack, F.M.G., Hou, D., 2021. A review of green remediation strategies for heavy metal contaminated soil. Soil Use Manage.
Wang, S.-L., Liu, C.H., Wang, M.K., Chuang, Y.H., Chiang, P.N., 2009. Arsenate adsorption by Mg/Al–NO3 layered double hydroxides with varying the Mg/Al ratio. Applied Clay Science 43, 79-85.
Wang, X., Bai, Z., Zhao, D., Chai, Y., Guo, M., Zhang, J., 2013. New synthetic route to Mg–Al–CO3 layered double hydroxide using magnesite. Materials Research Bulletin 48, 1228-1232.
Wang, Y., O'connor, D., Shen, Z., Lo, I.M., Tsang, D.C., Pehkonen, S., Pu, S., Hou, D., 2019. Green synthesis of nanoparticles for the remediation of

928 contaminated waters and soils: Constituents, synthesizing methods, and
929 influencing factors. Journal of Cleaner Production 226, 540-549.
930 Xu, S., Zhang, L.P., Zhao, J.W., Cheng, J., Yu, Q.Q., Zhang, S.W., Zhao, J.L.,
931 Qiu, X.H., 2020. Remediation of chromium-contaminated soil using
932 delaminated layered double hydroxides with different divalent metals.
933 Chemosphere 254, 11.
934 Yang, T., Zhang, Z., Zhang, F., Gao, Y., Wu, Q., 2020. Chloride and heavy metal
935 binding capacities of hydrotalcite-like phases formed in greener one-part
936 sodium carbonate-activated slag cements. Journal of Cleaner Production,
937 120047.
938 Yang, X., Wang, L., Guo, J., Wang, H., Mašek, O., Wang, H., Bolan, N.S., Alessi,
939 D.S., Hou, D., 2022. Aging features of metal(loid)s in biochar-amended soil:
940 Effects of biochar type and aging method. Sci. Total Environ. 815, 152922.
941 Ye, H., Liu, S., Yu, D., Zhou, X., Qin, L., Lai, C., Qin, F., Zhang, M., Chen, W.,
942 Chen, W., 2022. Regeneration mechanism, modification strategy, and
943 environment application of layered double hydroxides: Insights based on
944 memory effect. Coordination Chemistry Reviews 450, 214253.
945 Ye, J., Cheng, B., Wageh, S., Al-Ghamdi, A.A., Yu, J., 2016. Flexible Mg–Al
946 layered double hydroxide supported Pt on Al foil for use in room-temperature
947 catalytic decomposition of formaldehyde. Rsc Advances 6, 34280-34287.
948 Yi, X., Liang, X., Yingming, X., Xu, Q., Huang, Q., Lin, W., Yuebing, S., 2017.
949 Remediation of heavy metal-polluted agricultural soils using clay minerals: a
950 review. Pedosphere 27, 193-204.
951 Yi, Y., Liska, M., Jin, F., Al-Tabbaa, A., 2016. Mechanism of reactive magnesia–
952 ground granulated blastfurnace slag (GGBS) soil stabilization. Canadian
953 Geotechnical Journal 53, 773-782.
954 Yu, L., Qin, L., Sun, X., Wang, L., Chen, S., Wang, M., 2023. Intercropping with
955 herbs minimizes cadmium availability through altering physicochemical
956 dynamics and metabolite profiles in wheat rhizosphere. Soil Use and
957 Management 39, 645-658.
958 Yuan, Y., Garg, S., Ma, J., Waite, T.D., 2021. Kinetic Modeling-Assisted
959 Mechanistic Understanding of the Catalytic Ozonation Process Using Cu–Al
960 Layered Double Hydroxides and Copper Oxide Catalysts. Environmental
961 Science & Technology 55, 13274-13285.
962 Zeng, B., Wang, Q., Mo, L., Jin, F., Zhu, J., Tang, M., 2022. Synthesis of Mg-Al
963 LDH and its calcined form with natural materials for efficient Cr (VI) removal. J.
964 Environ. Chem. Eng. 10, 108605.
965 Zhang, J., Hou, D., Shen, Z., Jin, F., O'Connor, D., Pan, S., Ok, Y.S., Tsang,
966 D.C., Bolan, N.S., Alessi, D.S.J.E.R., 2020a. Effects of excessive impregnation,
967 magnesium content, and pyrolysis temperature on MgO-coated watermelon
968 rind biochar and its lead removal capacity. 183, 109152.
969 Zhang, S., Chen, J., Yu, J., Yu, Q., Qiu, X., 2022a. Remediation of Cd-
970 contaminated soil through different layered double hydroxides: The weakness
971 of delamination and mechanism. J. Environ. Chem. Eng. 10, 107815.

Zhang, W., Cheng, H., Peng, S., Li, D., Gao, H., Wang, D., 2020b. Performance and mechanisms of wastewater sludge conditioning with slag-based hydrotalcite-like minerals (Ca/Mg/Al-LDH). Water research 169, 115265.
Zhang, Y., Tan, X., Duan, G., Cui, J., Ren, M., Cao, J., Xu, C., Yang, W., Lin, A., 2022b. Magnesium slag for remediation of cadmium‐and arsenic‐contaminated paddy soil: A field study. Soil Use and Management 38, 1470-1480.
Zhao, S., Qin, L., Wang, L., Sun, X., Yu, L., Wang, M., Chen, S., 2022. Soil bacterial community responses to cadmium and lead stabilization during ecological restoration of an abandoned mine. Soil Use and Management 38, 1459-1469.
Zhong, K., Zhang, C., Ren, S., Huang, H., Rong, Q., Zhou, Y., 2021. Remediation of soil in a deserted arsenic plant site using synthesised MgAlFe-LDHs. Bulletin of Environmental Contamination and Toxicology 107, 167-174.
Zhou, H., Jiang, Z., Wei, S., 2018. A new hydrotalcite-like absorbent FeMnMg-LDH and its adsorption capacity for Pb2+ ions in water. Applied Clay Science 153, 29-37.
Zong, W., Wang, L., Wang, X., Geng, X., Lian, Y., Wang, H., Hou, R., Guo, J., Yang, X., Hou, D., 2023. Unraveling the aging dynamics in the simultaneous immobilization of soil metal (loid) s using oxides. Sci. Total Environ., 167220.
Zou, Y., Wang, X., Ai, Y., Liu, Y., Li, J., Ji, Y., Wang, X., 2016. Coagulation Behavior of Graphene Oxide on Nanocrystallined Mg/Al Layered Double Hydroxides: Batch Experimental and Theoretical Calculation Study. Environmental Science & Technology 50, 3658-3667.